Title

Studying Immunotherapy Resistance in a Melanoma Autologous Humanized Mouse Xenograft

Journal

Molecular Cancer Research, 19(2)

ISSN

1541-7786

Authors

Morton, J Jason
Alzofon, Nathaniel
Keysar, Stephen B
et al.

Publication Date

2021-02-01

DOI

10.1158/1541-7786.mcr-20-0686

Peer reviewed

HHS Public Access

Author manuscript

Mol Cancer Res. Author manuscript; available in PMC 2021 August 01.

Published in final edited form as:

Mol Cancer Res. 2021 February ; 19(2): 346–357. doi:10.1158/1541-7786.MCR-20-0686.

Studying immunotherapy resistance in a melanoma autologous humanized mouse xenograft.

J. Jason Morton[1], **Nathaniel Alzofon**[1], **Stephen B. Keysar**[1], **Tugs-Saikhan Chimed**[1], **Julie Reisinger**[1], **Loni Perrenoud**[1], **Phuong N. Le**[1], **Cera Nieto**[1], **Karina Gomez**[1], **Bettina Miller**[1], **Randi Yeager**[1], **Dexiang Gao**[2], **Aik-Choon Tan**[1,2], **Hilary Somerset**[3], **Theresa Medina**[1], **Xiao-Jing Wang**[3,4,5], **Jing H. Wang**[6], **William Robinson**[1], **Dennis R. Roop**[4], **Rene Gonzalez**[1], **Antonio Jimeno**[1,4]

[1]Division of Medical Oncology, Department of Medicine, University of Colorado School of Medicine, Aurora, CO, 80045, USA.

[2]Department of Biostatistics and Informatics, University of Colorado School of Medicine, Aurora, CO, 80045, USA.

[3]Department of Pathology, University of Colorado School of Medicine, Aurora, CO, 80045, USA.

[4]Charles C. Gates Center for Regenerative Medicine, University of Colorado School of Medicine, Aurora, CO, 80045, USA.

[5]Veterans Affairs Medical Center, VA Eastern Colorado Health Care System, 1700 N. Wheeling St., Aurora, CO, 80045, USA

[6]Department of Immunology and Microbiology, University of Colorado School of Medicine, Aurora, CO, 80045, USA.

Abstract

Resistance to immunotherapy is a significant challenge, and the scarcity of human models hinders the identification of the underlying mechanisms. To address this limitation, we constructed an autologous humanized mouse (aHM) model with hematopoietic stem and progenitor cells (HSPCs) and tumors from two melanoma patients progressing to immunotherapy. Unlike mismatched humanized mouse (mHM) models, generated from cord blood-derived HSPCs and tumors from different donors, the aHM recapitulates a patient-specific tumor microenvironment (TME). When patient tumors were implanted on aHM, mHM and NOD/SCID/IL2rg$^{-/-}$ (NSG) cohorts, tumors appeared earlier and grew faster on NSG and mHM cohorts. We observed that immune cells differentiating in the aHM were relatively more capable of circulating peripherally, invading into tumors and interacting with the TME. A heterologous, human leukocyte antigen

Correspondence Antonio Jimeno M.D., Ph. D., Professor of Medicine, University of Colorado School of Medicine. 12801 E. 17th Avenue, MS-8117, Aurora, CO 80045; Phone: 303-724-3808; Fax: 303-724-2478, Antonio.Jimeno@cuanschutz.edu.

Author contributions

Conceptualization and methodology, J.J.M., S.B.K., A.J.; Analysis, J.J.M., N.A., D.G., A.J.; Investigation/experimentation, J.J.M., J.R., L.P., P.N.L., T-S.C., R.Y., B.M.; Resources, A-C.T., H.S., T.M.; Writing – original draft, J.J.M., A.J.; Writing – review and editing, S.B.K., P.N.L., C.N., K.G., X-J.W., J.W., D.R.; Supervision, A.J., W.R., R.G.; Funding, A.J., J.J.M., X-J.W. All authors have reviewed the manuscript.

Conflict of Interest Disclosures

The authors declare no potential conflicts of interest.

(HLA-A) matched cohort also yielded slower growing tumors than non-HLA-matched mHM, indicating that a less permissive immune environment inhibits tumor progression. When the aHM, mHM, and NSG cohorts were treated with immunotherapies mirroring what the originating patients received, tumor growth in the aHM accelerated, similar to the progression observed in the patients. This rapid growth was associated with decreased immune cell infiltration, reduced interferon gamma (IFNγ)-related gene expression, and a reduction in STAT3 phosphorylation, events that were replicated *in vitro* using tumor-derived cell lines.

Implications: Engrafted adult HSPCs give rise to more tumor infiltrative immune cells, increased HLA matching leads to slower tumor initiation and growth, and continuing immunotherapy past progression can paradoxically lead to increased growth.

INTRODUCTION

Increased scrutiny of the tumor microenvironment (TME) has led to better understanding of pro- and anti-tumor TME components and the development of therapies aimed at disrupting the mechanisms underlying immune evasion in human cancer. The cytotoxic T-lymphocyte-associated protein 4 (CTLA4) inhibitor ipilimumab was approved for the treatment of metastatic melanoma in 2011; the programmed cell death protein 1 (PD-1) inhibitors nivolumab and pembrolizumab followed in 2014 and 2015, respectively (1-3). However, immune-directed therapy is often limited by intrinsic and acquired tumor resistance and an improved understanding of these phenomena is an acute need. Such resistance has been associated with mutations in genes encoding interferon gamma (IFNγ), the Jak-STAT signaling pathway (4, 5) and with changes in PD-L1 and HLA expression that reduce the effectiveness of anti-PD-1 therapies in promoting an anti-tumor T cell response (6, 7).

In addition, the phenomenon of immunotherapy-induced tumor hyperprogression has been recently identified and described in a subset (~9%) of cancer patients (8). Characterized by a sudden increase in the rate of tumor growth after the start of immunotherapy, hyperprogression has been observed in several types of cancer, including melanoma. It is often associated with mutations or acquired dysregulation in the genes encoding MDM2/4, EGFR, DMNT3A, JAK1/2, and B2M (9, 10). Many of these genes are associated with the IFNγ pathway (11, 12). Since it is difficult to quantitatively compare pre-treatment tumor growth with that observed after immunotherapy, and given the lack of appropriate laboratory models, a comprehensive examination of hyperprogression has been thus far challenging.

Since a human TME cannot be examined when cancer xenografts are grown on traditional immunodeficient animal models, humanized mouse (HM) patient-derived xenograft (PDX) models have been developed. HM, engrafted with the hematopoietic precursor and stem cells (HSPCs) necessary for the development of a functional human immune system, can be used to examine the complex relationships in the TME within the context of a growing and invading tumor. We previously generated an HM xenograft model of head and neck squamous cancer and have shown that the engrafted HSPCs can divide, differentiate, and invade implanted tumors, where they alter the expression of immune-related genes to more closely match the profiles found in the originating patient tumors (13, 14). Because these early models were created from donated umbilical cord blood, the resultant immune system

and subsequently implanted xenograft came from separate sources (thus termed mismatched HM, or mHM), and the interactions of immune cells and tumor tissues may not accurately mirror those found in the originating patients.

In the current study we: (a) generated an autologous humanized mouse (aHM) model made from the HSPCs and tumor tissue collected from two metastatic melanoma patients (CUHM003 and CUHM005) after progression during immune-directed therapy, (b) determined differences in tumor formation and growth between aHM and non-humanized NOD/SCID/IL2rg$^{-/-}$ (NSG) and mHM cohorts, (c) replicated the treatment received by the patients to identify patterns of growth in each model, and (d) characterized the molecular and immune events associated with immune-directed therapy. We observed a distinct pattern of immune cell engraftment in the aHM, and in this model tumor growth, immune cell infiltration, and response to CTLA4- and PD-1 inhibitors were more consistent with what was observed in the corresponding patients (15, 16). Finally, molecular analyses revealed altered transcription among IFNγ-related genes associated with hyperprogression. Both mHM and aHM models provide humanized TMEs in which patient tumors can be grown and studied, however aHM afford unique opportunities to study the factors driving tumor progression and hyperprogression.

MATERIALS AND METHODS

HSPC collection, expansion, and engraftment in mice

De-identified cord blood was obtained from the University of Colorado cord blood bank (http://www.clinimmune.com/cordbloodbank/). The use of human subjects was approved by the Colorado Multiple Institutional Review Board (COMIRB #14-0842). Eligible, willing patients with incurable melanoma were prospectively enrolled, had a fresh tumor biopsy, and received filgrastim (10 μg/kg daily) for four days. A total of 150 mL of blood was collected 4-6 days later.

HSPCs were purified from either cord or patient blood by CD34+ positive cell selection (Stemcell Technologies, Vancouver, BC; Cat#14756), suspended in serum-free expansion medium (Stemcell Technologies, Cat#09650), and cultured at 37°C, 5% CO_2 for 5-8 days. Cells were characterized by cytometry, using CD34, CD45, CD73, and CD166 antibodies (Biolegend, San Diego, CA; Cat#343608, RRID:AB_2228972; 304039, RRID:AB_2562057; 344006, RRID:AB_1877157; 343904, RRID:AB_2289302) at a 1:10 concentration. NSG (Jackson Laboratories, Bar Harbor, ME; Cat#005557, RRID:IMSR_JAX:005557) mice were primed for engraftment by 1.5 Gy whole-body irradiation. After a recovery of 4-6 hours, the mHM mice were each injected with 400,000 expanded CD34+ cells, suspended in 0.2 mL sterile PBS. The aHM003 mice received 150,000 CD34+ cells, while the aHM005 mice received 140,000 CD34+ cells. When present, MSC-like cells were added to comprise 5% of the total injected cells. The mice were bled via the tail vein after 8 – 10 weeks to assess HSPC engraftment. Their peripheral blood was analyzed by flow cytometry, using human CD3, CD11b, CD19 and/or CD45 (Biolegend; Cat#300312, RRID:AB_314048; 301310, RRID:AB_314162; 392504, RRID:AB_2728416; 304039; RRID:AB_2562057) antibodies at 1:10. At the conclusion of the study, HM bone marrow was collected and analyzed by flow cytometry, using human

CD34 and CD45 antibodies at 1:10. The University of Colorado Institutional Animal Care and Use Committee (IACUC) approved all experiments involving mice. PDX generation and animal care have been previously reported (17).

In vivo treatment studies

CUHM003 mice received either a human IgG control (Gammagard; Takeda, Lexington,MA; 10mg/kg), ipilimumab (Bristol-Myers Squibb, New York; 20 mg/kg), or pembrolizumab (Merck, Kenilworth, NJ; 20 mg/kg). CUHM005 mice received IgG control (10 mg/kg), ipilimumab, nivolumab (Bristol-Myers Squibb; 10 mg/kg), or ipilimumab plus nivolumab, each given at the single-agent dose. Tumors were measured three times weekly, and when tumors averaged 75mm^3 treatment was administered twice weekly by intraperitoneal injection for four weeks. At the end of study, blood was collected by cardiac puncture in EDTA. Tissues were collected for cytometry, flash frozen in liquid nitrogen, and in placed in formalin to paraffin-embed.

Fluorescence activated cell sorting (FACS) and flow cytometry

Tumor and mouse tissues were prepared for cytometric analysis as previously described (14). Cell sorting was performed using a MoFlo XDP (Beckman Coulter, Fort Collins, CO), and flow cytometry was completed on a CyAn ADP (Beckman Coulter) using Summit V5.1 (Beckman Coulter) software.

Immunohistochemistry (IHC)

IHC analyses were performed as described (13). Primary antibodies and dilutions: CD45 (Dako; Cat#M0701, RRID:AB_2661839) 1:100; CD3 (Abcam; San Francisco, CA; Cat#ab5690, RRID:AB_305055), 1:500; CD19 (MyBiosource; San Diego, CA; Cat#MBS2544305, RRID:AB_2868606), 1:100; and CD68 (Dako; Cat#M0876, RRID:AB_2074844) 1:100. Staining was developed using the following conditions: EnVision + Dual Link System HRP (Dako; Cat#K4061) for 30 minutes and substrate-chromogen (DAB+) Solution (Dako; Cat#K3468) for 5 minutes. Slides were then counterstained with Automated Hematoxylin (Dako; Cat#S3301) for 10 minutes.

Exome and mRNA Sequencing and Bioinformatics

Biological duplicates were sent to the UCCC Genomics and Microarray Core for library generation and Illumina HiSeq (Illumina, San Diego, CA) sequencing. FastQC (v0.11.3, RRID:SCR_014583) was used for quality control (Exome-seq and RNA-seq). Cutadapt (v1.8.1, RRID:SCR_011841) was used to remove Illumina adapters. Trimmomatic (v0.33, RRID:SCR_011848) was used to remove low quality reads (18). Exome variants were called using the IMPACT pipeline (19) to annotate somatic and non-common (with allele frequency greater than 1% in dbSNP, RRID:SCR_002338 (20) or the 1000 Genomes Project, RRID:SCR_008801 (21)) variants. Transcript reads were quantified using Tuxedo Suite (http://cole-trapnell-lab.github.io/projects/) (22), aligned against the GRCh37 reference genome using TopHat (v2.0.14, RRID:SCR_013035), and assembled and merged using Cufflinks (v2.2.1, RRID:SCR_014597). Gene set enrichment analysis (GSEA2-2.2.0, RRID:SCR_003199) was conducted using MSigDB (v5.2, http://software.broadinstitute.org/

gsea/msigdb/collections.jsp) (23, 24). Pathways were analyzed using GSEABase R package v1.48.0 and ClusterProfiler v3.14.2, RRID:SCR_016884 (25) and were considered highly significant at an FDR q-value ≤ 0.01, significant at q ≤ 0.05, and modestly significant at the default threshold value of q ≤ 0.25. Differential expression was analyzed using DESeq2 with APEGLM shrinkage estimator with an FDR of 0.1 (26). Top pathways/gene ontologies were identified using DAVID, RRID:SCR_001881 (27, 28).

Cell line generation and sphere assay

Cell lines were derived from tumor tissue using RMK media, as described (29), and validated by Mycoplasma testing and STR analysis (2018-03-18 for CUHM003 and 2018-05-03 for CUHM005). 200,000 cells per well were plated in triplicate in ultra-low attachment 12-well plates and supplemented with media after 4, 7, and 10 days. T cells were isolated by magnetic separation and activated (Stemcell Technologies; Cat#19051, 10971) from 5mL de-identified adult blood draws acquired through the University of Colorado. Cells were allowed to form spheres for 10 days before 20,000 T cells, 2ng/mL purified interferon gamma (R&D Systems, Minneapolis, MN; Cat# 285-IF-100), and/or 4μg/mL pembrolizumab or nivolumab were added. Spheres were imaged, counted, and measured using a Zeiss Axio Observer Z1 inverted microscope (Zeiss software Rel. 4.8). siIFNγR2 knock-down was verified by qPCR as described (29).

Cell line siRNA experiments

For IFNγR2 and STAT3 knock-downs, cells were seeded in 6 well plates and incubated for 24 hours. Media was replaced with serum-free DMEM for 30 minutes prior to transfection with 1 μl/ml Dharmafect1 and 50-100 nM siRNA (GE Dharmacon, Lafayette, CO; IFNγR2 SMARTpool J-012713-05 – 08; STAT3 SMARTpool J-003544-07 – 10). Cells were incubated for 24 hours before DMEM containing 20% FBS was added, and cells were incubated for another 48-72 hours.

Cytokine arrays

Plasma from mouse blood was collected and flash frozen for subsequent analysis. Cytokine presence and concentration in the plasma was interrogated on a human cytokine array kit (R&D Systems; Cat# ARY005B) according to the manufacturer's instructions. Cytokine concentration was quantified by ImageJ software, version 1.5, RRID:SCR_003070 (National Institutes of Health, imagej.nih.gov), and visualized using R.

Protein isolation and western blotting

Western blotting and analysis were conducted as previously described (30). Primary antibodies and dilutions: 1:2000 Actin (pan) (Cell Signaling, Danvers, MA; Cat#4968, RRID:AB_2313904), 1:1000 phospho-STAT1 (Cell Signaling; Cat#9167, RRID:AB_561284), 1:1000 STAT1 (Cell Signaling; Cat#9175, RRID:AB_2197984), 1:1000 phospho-STAT3 (Cell Signaling; Cat#9131, RRID:AB_331586), 1:2000 STAT3 (Cell Signaling; Cat#4904, RRID:AB_331269). Secondary anti-rabbit IgG (Jackson ImmunoResearch, West Grove, PA; Cat#111-035-045, RRID:AB_2337938), and used at a

1:5,000 dilution. Quantification of relative protein levels was completed using ImageJ, RRID:SCR_003070.

Statistics

In vitro and *in vivo* (using ≥5 mice/group) experiments were compared with Brown-Forsythe ANOVAs and two-sided t tests. Final tumor volumes for all tumor groups were calculated as the fold change in size between the beginning and end of the study after the initial volumes of the tumors had been set at a value of 1. When treatment groups were compared, the treated arms were all normalized by the average fold change of the associated control tumors, as previously described (31). Spheroids were compared using standard ANOVAs and Dunnett's multiple comparison tests. Calculations were done using GraphPad Prism, RRID:SCR_002798, version 8.3. Data are represented graphically as mean ±SEM. GSEA estimates the statistical significance of the enrichment scores by a two-sided modified Kolmogorov-Smirnov permutation test. P and Q values of less than 0.05 were statistically significant. All statistical tests were two-sided.

RESULTS

HSPCs from cord and patient blood expand *ex vivo* and engraft mHM and aHM cohorts

In order to conduct a comprehensive comparison, we generated a non-humanized model (NSG), a model with a mismatched immune system (mHM), and a model with an autologous immune system (aHM) (Figure 1A) for both CUHM003 and CUHM005 patients. To generate the aHM cohorts, we isolated HSPCs from G-CSF-stimulated patient blood. To construct mHM cohorts, we isolated HSPCs from donated cord blood. The CD34+ HSPCs were then expanded *ex vivo* for ~8 days, after which the number of patient cells had undergone an average ~40-fold expansion (Figure 1B; Supplemental Table 1) and the cord blood cells had increased by ~180-fold. We also observed and expanded a separate population of adherent CD73-CD166+ cells, characteristic of mesenchymal stem cells (MSCs) (14). Since it has been demonstrated that radiation-induced damage to bone marrow encourages HSC homing and establishment in this niche (32), we injected expanded HSPCs and MSCs into the tail veins of sub-lethally irradiated NSG mice to create mHM and aHM cohorts. In order to generate enough mice to reproduce patient therapy, each mHM received 400,000 HSPCs, and each aHM was engrafted with 140,000 HSPCs, a population at the lower end of what is necessary for successful humanization using cord blood HSPCs (14). We hypothesized that increased HLA matching would enhance the functional efficiency of the mature immune cells produced by the HSPCs in recognizing and interacting with implanted autologous tumor tissue and decrease the required number of HSPCs in these models. A similar phenomenon has been observed in patients receiving cord blood transplants, where a reduced mismatch (1 vs 2 HLA) requires fewer total nucleated cells ($>2.5 \times 10^7$/kg vs $>5.0 \times 10^7$/kg) to achieve similar engraftment and clinical outcomes (33).

After eight weeks, we identified a population of human B cells, comprising 0.01-0.4% of the total white blood cells (WBCs), in the mouse peripheral blood (Supplemental Figure 1). We also quantified the human blood cell populations in the mouse bone marrow, blood, and spleen by cytometry at the conclusion of the studies (Supplemental Figure 2). On average,

the bone marrow of the mHM cohorts contained healthy populations of human CD45+ immune cells (mHM003 – 12.37%, mHM005 – 27.93% of all bone marrow cells) and smaller populations of HSPCs (mHM003 – 0.94%, mHM005 – 3.73%). The bone marrow of the aHM cohorts contained more modest CD45+ cell populations (aHM003 – 0.29%, aHM005 – 0.04%) and HSPC (aHM003 – 0.03%, aHM005 - <0.01%; Supplemental Table 2), possibly reflecting the lower initial HSPC injection numbers. We also compared human CD45+ cells within mHM and aHM bone marrow and spleen by immunohistochemistry (IHC; Figure 1C, Supplemental Figure 3) and observed similar patterns of human CD45+ cell engraftment.

Delayed tumor initiation and decreased growth in aHM and in HLA A-matched HM

Approximately ten weeks after their humanization, tumors were implanted on both flanks and a shoulder of the NSG, mHM, and aHM cohorts, using expanded tumor tissue from the initial biopsy. Tumors appeared earlier and grew faster on the NSG and mHM cohorts. At study end, NSG003 tumors were 1.4 times larger than those in aHM003 ($p=0.04$) (Figure 2A). NSG005 and mHM005 tumors were 3.0-fold ($p<0.01$) and 3.3-fold ($p<0.01$) larger than aHM005, respectively (Figure 2B). There was no difference in the rate of growth between the NSG and mHM tumors in CUHM003 or CUHM005. In order to further investigate immune matching, we implanted CUHM003 tumors on NSG, HM HLA-A-mismatched (mHM003b), and HM HLA-A-matched cohorts (mHM003-HLA). Tumor occurrence was again delayed and growth trended slower (but without reaching statistical significance) in mHM003-HLA *versus* that observed in NSG003 and mHM003b cohorts (Supplemental Figure 4A), suggesting that immune permissiveness modulates tumor occurrence and growth.

Tumor growth accelerates in aHM treated with checkpoint inhibitors

Prior to trial enrollment and tumor biopsy the CUHM003 patient had been treated with ipilimumab, initially achieving a partial response before progressing, and then pembrolizumab, resulting in rapidly progressive disease. We conducted a three-arm study (control, ipilimumab, pembrolizumab) on the NSG003, mHM003, and aHM003 tumor-bearing mice. We observed no growth differences between NSG003 and mHM003 tumors. There were 2-fold and 4-fold increases in the growth of aHM003 ipilimumab- and pembrolizumab-treated tumors compared to controls (ANOVA $p=0.06$; T-test $p=0.02$ and $p=0.08$, respectively; Figure 2C; Supplemental Figure 4B).

The CUHM005 patient had exhibited rapid progressive disease during combined therapy with ipilimumab and nivolumab (a PD-1 inhibitor) given prior to humanized trial enrollment and tumor biopsy. We conducted a four-arm study (control, ipilimumab, nivolumab, combination) on NSG005, mHM005, and aHM005 mice (Figure 2D; Supplemental Figures 4C and 5). We observed no difference in the growth of the treated NSG005 or mMH005 groups, but a significant acceleration in the growth of the nivolumab- and combination-treated aHM005 tumors occurred (2- and 3-fold increase; ANOVA $p<0.01$; T-test $p=0.02$ and $p<0.01$, respectively).

aHM tumors show a distinct pattern of infiltration by immune cells

To determine the basis for this phenomenon, we analyzed the pattern of human immune cell invasion in fresh tumor samples by cytometry (Supplemental Figure 6) and in paraffin-embedded tumors by IHC (Supplemental Figure 7). Compared to their originating patient samples, melanoma tumors on HM contained less stroma and fewer infiltrating human immune cells. Cytometric analysis, however, indicated that small populations of human T cells, B cells, and macrophages similarly infiltrated the tumors in both mHM and aHM – a noteworthy observation considering the relatively lower bone marrow engraftment observed in the aHM models. When normalized by the percentage of human cells in the bone marrow, relative T cell presence in aHM003 was nearly eight times greater than in mHM003, while there were 2000 times more tumor-infiltrating T cells in aHM005 than in mHM005, indicating that autologous T cells have a greater capacity to interact with tumor tissue, even though this infiltrative capacity decreased upon immunotherapy treatment (Table 1). IHC revealed that the human immune cells were generally congregated at the tumor capsule, implying that their association with the tumor is especially transient, as has been described for immunotherapy-refractory melanoma when comparing pre- and post-immunotherapy tumor samples from both patients (Supplemental Figure 7), where the relatively few T cells present lacked infiltrative capacity and accumulated mainly near the tumor capsule (15, 16).

Whole exome sequencing identifies known mutations associated with growth regulation

In order to identify genetic alterations associated with these observations, we identified 281 nonsynonymous gene mutations in CUHM003 patient's tumor (Supplemental Table 3A). By the time of tumor progression after immunotherapy, mutations in 187 additional genes were present (Supplemental Table 3B). There were mutations in 99 genes in the CUHM005 patient tumor at diagnosis and 262 additional gene mutations upon progression (Supplemental Table 3C-D). Since neither of these patients initially responded to a PD-1 inhibitor, we identified mutant genes present in both tumors which might be relevant to the observed treatment failure. At diagnosis, the tumors shared mutations in 11 genes (Supplemental Figure 8A), and after progression, they shared an additional 64 mutations (highlighted in Supplemental Tables 3A-D). Of these genes, known *NRAS* mutations, previously described in the Catalogue of Somatic Mutations in Cancer (COSMIC) and shown to be activating and oncogenic, seemed particularly noteworthy (Supplemental Figure 8B) (34). Although there is some correlation between *NRAS* mutations and a response to a PD-1 inhibitor (35), mutations in *NRAS* are also known to activate the transcription factor STAT3, a downstream component of the IFNγ-stimulated Jak-STAT pathway and may be associated with rapid tumor growth after anti-PD-1 treatment (36).

Transcriptome analyses defines a specific response to interferon stimulation in aHM tumors

We next examined RNA expression in these tumors by next-generation sequencing. When genes expressed only in the HM and corresponding patient tumors were analyzed using the NIH Database for Annotation, Visualization and Integrated Discovery (DAVID), the transcriptomes of both CUHM003 and CUHM005 humanized mice tumors were enriched in immunity-related genes, as previously observed (Supplemental Table 4, Supplemental

Tables 5A-D) (13). No significant differences in the transcriptomic fingerprint between mHM and aHM tumors existed (differential expression analysis; adjusted p-value=0.006), an observation which supports the higher relative activity of aHM immune cells, given the differential engraftment in the mHM and aHM cohorts.

To investigate the basis for the accelerated growth in the treated aHM tumors, we analyzed GSEA hallmarks, comparing the patient tumor to and between the NSG, mHM, and aHM models (Supplemental Figure 9, Supplemental Table 6). The IFNα and IFNγ hallmarks were uniquely upregulated in untreated aHM003 tumors, indicating their expression reverts to a more similar state to that observed in the patient. We next observed that CTLA4 and/or PD-1 inhibition resulted in upregulation of IFNα and IFNγ pathways in both NSG003 and NSG005 as well as upregulation of IFNα in mHM003 (Figure 3A). In contrast, CTLA4 and/or PD-1 inhibition led to downregulation of IFNα and IFNγ pathways in aHM003 and aHM005 tumors (Figure 3A, Supplemental Table 7). A comparison of the normalized enrichment score (NES) of the GSEA hallmarks between control and PD-1 inhibitor-treated tumors depicts the reduction in the IFNα hallmark after treatment in aHM003, while both IFNα and IFNγ are downregulated in mHM005 and aHM005 (Figure 3B). In CUHM005 tumors after combination treatment, only the EMT and TNFα pathways rise in aHM005 compared to NSG005 and/or mHM005 (Figure 3C), suggesting IFN signaling is specifically modulated by PD-1 inhibition.

Unbiased analyses using the Kyoto Encyclopedia of Genes and Genomes (KEGG) revealed both positively and negatively enriched components on the IFNγ and Jak-STAT pathways (Supplemental Figure 10A-B). DAVID analyses showed enrichment in chemokine signaling pathway genes (p=0.01) in aHM003, while the expression of genes participating in the PI3K-Akt and IFNγ signaling pathways was enriched in aHM005 ($p<0.05$; Supplemental Tables 8A-B). Heatmaps of these genesets emphasize the bidirectional change in expression in aHM tumors (Supplemental Figure 10C), supporting the role of the IFNγ pathway in mediating tumor growth in response to PD-1 inhibition.

Ex vivo analysis with tumor-derived cell lines

To investigate the basis of the differential response to anti-PD-1 treatment in the aHM tumors, and given the limitation to establishing further aHM cohorts, we established cell lines from early passages of the CUHM003 and CUHM005 PDX by cell sorting. Since *in vivo* growth corresponded with reduced T cell presence, we replicated the conditions caused by this phenomenon by transfecting both cell lines with an siRNA construct against the IFNγ receptor (IFNγR2; Supplemental Figure 11), thereby desensitizing cells to the IFNγ produced by active T cells. We seeded 200,000 cells on low-adherence plates to encourage spheroid formation. Under baseline conditions, both cell lines behaved similarly: the addition of purified IFNγ had minimal effect on final spheroid size, but knockdown of IFNγR2 dramatically increased their size (CUHM003 $p<0.001$, CUHM005 p=0.006; Figure 4A). The addition of activated T cells led to a slight increase in average spheroid size, blunting the inhibitory effect of IFNγR2 knockdown (Figure 4B). The addition of a PD-1 inhibitor did not further affect sphere size (Figure 4C-D; representative images in Figure 4E), indicating that cell growth for both CUHM003 and CUHM005 is directed primarily by

the presence of a functioning IFNγR2, and that IFNγ depletion (either by disappearance of autologous T cells or by absence of its receptor) increases cell growth.

To dissect intracellular signaling associated with IFNγ, we interrogated STAT1 and STAT3, since these are the primary cellular mediators of extracellular IFNγ and both modulate cancer growth (37). The ratio of STAT3/STAT1 RNAseq transcripts closely mirrored the tumor growth rates (Figure 5A) although, much as observed during our analysis of the changes in the GSEA hallmarks (Figure 3C), additional signals appear to have a role in driving tumor growth in the CUHM005 aHM combination tumor. The transcription of STAT1- and STAT3-dependent genes with or without PD-1 inhibitor across mouse model tumors showed that STAT1-mediated transcription dropped while STAT3-mediated transcription increased only in aHM tumors (Figure 5B). Since STAT3 is abundantly expressed and thus difficult to quantify, we examined its role using tumor-derived cell lines in which a transfected siSTAT3 construct reduced its expression. In accordance with our observations using IFNγR2 knock-downs, we observed that the addition of exogenous IFNγ to these CUHM003 and CUHM005 cell lines led to a notable increase in pSTAT1 expression and a decrease in pSTAT3 expression (Figure 5C-D; cell lines), the combination of which would inhibit cellular proliferation. We observed a similar reduction in pSTAT3 in PD-1-inhibitor treated aHM tumors, although it was uniquely coupled to a concurrent pSTAT1 reduction (Figure 5C-D; CUHM003-CUHM005), creating a distinct environment in which cellular proliferation increased without pSTAT3 activation. A cytokine array comparing mHM and aHM plasma from mice with PD-1 inhibitor treated CUHM003 and CUHM005 tumors provides a possible clue to the mechanism driving this proliferation (Supplemental Figure 12). The chemokine CXCL12, whose downregulation has been previously shown to directly activate MAPK signaling in NRAS-mutated melanoma, is markedly reduced in PD-1 inhibitor treated aHM plasma (38). We can recapitulate such a regulatory environment in the cell lines in which the JAK-STAT pathway has been activated by IFNγ and in which STAT3 transcription has been reduced (Figure 5D; comparing the reduction in pSTAT3 expression after IFNγ+siSTAT3 treatment in the cell lines with that observed after PD-1 inhibition in the tumors).

DISCUSSION

The discovery of immunotherapies targeting CTLA4 and PD-1 is largely responsible for the improvement of metastatic melanoma outcomes, where one-year survival rates went from less than 25% (39) to between 47% and 63% (40, 41). These successes have paved the way in deploying these therapies in other tumor types, such as lung, colon, bladder, and head and neck cancers (42). Although effective, only 30-40% of patients respond to immune-directed treatment and even responders will often eventually acquire resistance (43). Furthermore, recent evidence indicates that these immunotherapies can prompt a rapid acceleration in tumor growth, a condition known as hyperprogression (8, 9). Although there has been some initial success in HM created from patient peripheral lymphocytes and tumor tissue (44, 45), no model exists in which treatment effectiveness can be predicted, and where the basis of tumor response can be explored (46). The aHM PDX model reported here addresses some of those limitations.

The aHM is based on the initial mHM models (13, 14) that were first deployed to study the relationship between an implanted tumor and the engrafted human immune system of the host mouse. Using the mHM, we showed that human immune cells infiltrated the tumor, upregulated human cytokine production, and partially reversed the expression in many of the tumor's immune-, EMT-, and extracellular matrix-related genes (13). We also demonstrated that this environment was responsive to immune modulation, and we observed that adequate humanization was required to achieve *in vivo* efficacy with PD-1 inhibitors (14). However, since mHM were generated from donated cord blood, the engrafted immune system is allogeneic with the implanted tumor tissue, a significant caveat in faithfully representing immune-directed therapy results or in guiding patient therapy. An HLA-matched immune system is uniquely necessary to prevent indiscriminate immune cell attack after xenograft implantation (47, 48). A more elegant technology is needed to recapitulate an immune system in an HM PDX model (49).

To address these caveats, we generated an aHM model using HSPCs isolated from the blood of metastatic melanoma patients. The development of the aHM in melanoma was driven by the relevance of immunity in melanoma, the accessibility of tissue for PDX generation, and the possibility of validating immunotherapy results against those observed in the originating patients. We also identified and cultured a second population of cells within these HSPCs with characteristics of mesenchymal stems cells (MSCs), since the presence of MSCs within cultured HSPCs promotes superior mouse engraftment and increase immune system reconstitution (50, 51). This process has previously been shown to double the human precursors in the bone marrow of mHM and increase by over 10-fold the circulating immune cells and tumor infiltrating T cells (14).

A first notable conclusion from this work is that the engraftment of patient HSPCs gave rise to an aHM model in which fewer HSPCs produced more active immune cells, as seen in clinical settings (33). Smaller numbers of autologous human cells were capable of changing the gene expression of implanted tumors. This indicates that the size of the human cell population may not be the only factor in determining humanization, and an autologous source of HSPCs may be critical in determining both engraftment and functionality. These differences in HSPC origin have profound implications in the deployment of aHM models, and their feasibility to further personalized therapies.

A second critical observation is that tumorigenicity was significantly diminished in aHM models. In immunotherapy-refractory melanoma, T cell invasion decreases and a switch to an "immune cold" TME is a hallmark of tumor progression and unresponsiveness to immunotherapy. The mHM003 and mHM005 cohorts had prominent populations of human CD45+ cells, and their tumors had significant T cell infiltration, but this had little effect on their growth (compared to NSG controls). Conversely, even though aHM003 and aHM005 had fewer circulating human immune cells, tumors on these mice appeared later and grew more slowly, as did those implanted on mHM003-HLA cohorts. This differential growth may be a consequence of varying immune cell activity within these models, suggesting that even partially effective immune surveillance leads to a delay in tumor formation and a lag in subsequent growth.

A third key finding is the immunotherapy-dependent accelerated tumor growth in aHM models, which can help identify factors responsible for tumor resistance or hyperprogression in patients. The expression of IFNγ-related pathways was highest in untreated aHM tumors but markedly reduced after treatment with PD-1 inhibitors, concordant with a relative decrease in infiltrating immune cells, when compared to those in the corresponding mHM models. This suggests that the rapid growth observed in these tumors was likely a consequence of the immunotherapy-induced disruption of a small population of active T cells. The basis of this paradoxical effect remains unidentified, but a similar reduction in T cells was observed in post-treatment patient tissues.

It remains unclear whether the treatment-induced tumor growth in the aHM represents true patient hyperprogression or is simply reminiscent of the rapid progression of both patients subsequent to their treatment, since the tumor tissue and patient HSPCs were acquired after the patients had demonstrated resistance to both CTLA4 and PD-1 inhibitors. Even though therapy was suspended after the onset of rapid progression and before either patient exhibited a classic hyperprogressive profile, growth of both of their tumors accelerated markedly after treatment. Hyperprogression was, however, observed in the majority of treated tumors in both aHM cohorts of a well-controlled study, and it is unlikely to be a coincidental effect. This type of comparison has not previously been possible, given the absence of suitable animal models.

To guide our investigation of the mechanism driving this treatment-induced growth, we derived cell lines from both melanoma patients. Analysis of comprehensive spheroid experiments strongly indicates that their growth is regulated by IFNγ. When the IFNγR2 receptor was knocked down, cells increased their growth, mirroring the *in vivo* observation that a PD-1 inhibitor reduced T cell presence and facilitated subsequent tumor progression. Likewise, our observation that pSTAT3 falls when exogenous IFNγ cannot stimulate the STAT3 phosphorylation in CUHM003 and CUHM005 siSTAT3 cell lines mirrors how pSTAT3 falls in response to a PD-1 inhibitor in aHM and highlights the role of IFNγ and Jak-STAT signaling in the rapid tumor growth observed in aHM. The notable reduction in CXCL12 in aHM tumors treated with a PD-1 inhibitor implies that this rapid growth may be driven by NRAS-mediated MAPK activation. Such a model is appealing, since CXCR4-CXCL12 signaling can be mediated by T cells, which we have shown to have increased activity in the aHM model. Their withdrawal from the TME subsequent to treatment with a PD-1 inhibitor would not only reduce IFNγ presence but would abrogate CXCR4-CXCL12 signaling, decreasing Jak-STAT pathway activity and removing its checks on MAPK signaling via the mutated NRAS present in these tumors (38, 52). This idea may also explain why STAT3-dependent genes are still elevated in aHM tumors when STAT3 phosphorylation has decreased, since many of these genes can also be regulated through the MAPK pathway (Figure 5B vs Figure 5D). Work towards elucidating the molecular mechanism driving this phenomenon is ongoing in aHM models.

A more complete understanding of TME environment in the aHM model will increase our understanding of immunotherapy resistance and tumor hyperprogression observed in cancer patients. It is also crucial that additional aHM PDX models be constructed in order to compare their tumor growth with that of treatment naïve or susceptible patients. These

results support the development and use of the aHM model, showing that it can recapitulate many aspects of the patient TME and also be used to examine uncharacterized tumor growth dynamics. The aHM reported here led to three noteworthy observations: even when created utilizing fewer adult patient-derived HSPCs and with less bone marrow engraftment, aHM gave rise to proportionally more circulating and tumor infiltrative immune cells than cord-blood derived mHM; greater HLA matching between immune cells and the tumor resulted in slower tumor initiation and growth; and tumors engrafted at the time of progression to immune therapy can paradoxically respond with increased growth upon continuing exposure to such therapy.

Supplementary Material

Refer to Web version on PubMed Central for supplementary material.

ACKNOWLEDGEMENTS

The authors wish to thank the patients who donated their tissue, blood, and time, and to the clinical teams who facilitated patient informed consent, as well as sample and data acquisition.

Financial Support

This work was primarily supported by National Institutes of Health grants R01CA149456 (A. Jimeno), R01CA213102 (A. Jimeno), R01DE024371 (A. Jimeno and X-J. Wang), P30-CA046934 (University of Colorado Cancer Center Support Grant), P30-AR057212 (University of Colorado Skin Diseases Research Center Support Grant), Ruth L. Kirschstein National Research Service Award T32CA17468 (X-J. Wang; P.N. Le, trainee), Training in Otolaryngology Research T32DC012280 (C. Nieto, trainee), ACS-IRG 16-184-56 Institutional American Cancer Society (J. Morton), the Daniel and Janet Mordecai Foundation (A. Jimeno), the Karsh family Foundation (A. Jimeno), and the Peter and Rhonda Grant Foundation (A. Jimeno).

REFERENCES

1. Hodi FS, O'Day SJ, McDermott DF, Weber RW, Sosman JA, Haanen JB, et al. Improved survival with ipilimumab in patients with metastatic melanoma. The New England journal of medicine. 2010;363(8):711–23. [PubMed: 20525992]
2. Barone A, Hazarika M, Theoret MR, Mishra-Kalyani P, Chen H, He K, et al. FDA Approval Summary: Pembrolizumab for the Treatment of Patients with Unresectable or Metastatic Melanoma. Clinical cancer research : an official journal of the American Association for Cancer Research. 2017;23(19):5661–5. [PubMed: 28179454]
3. Hazarika M, Chuk MK, Theoret MR, Mushti S, He K, Weis SL, et al. U.S. FDA Approval Summary: Nivolumab for Treatment of Unresectable or Metastatic Melanoma Following Progression on Ipilimumab. Clinical cancer research : an official journal of the American Association for Cancer Research. 2017;23(14):3484–8. [PubMed: 28087644]
4. Shin DS, Zaretsky JM, Escuin-Ordinas H, Garcia-Diaz A, Hu-Lieskovan S, Kalbasi A, et al. Primary Resistance to PD-1 Blockade Mediated by JAK1/2 Mutations. Cancer Discov. 2017;7(2):188–201. [PubMed: 27903500]
5. Luo N, Formisano L, Gonzalez-Ericsson PI, Sanchez V, Dean PT, Opalenik SR, et al. Melanoma response to anti-PD-L1 immunotherapy requires JAK1 signaling, but not JAK2. Oncoimmunology. 2018;7(6):e1438106. [PubMed: 29872580]
6. Ayers M, Lunceford J, Nebozhyn M, Murphy E, Loboda A, Kaufman DR, et al. IFN-gamma-related mRNA profile predicts clinical response to PD-1 blockade. The Journal of clinical investigation. 2017;127(8):2930–40. [PubMed: 28650338]
7. Manguso RT, Pope HW, Zimmer MD, Brown FD, Yates KB, Miller BC, et al. In vivo CRISPR screening identifies Ptpn2 as a cancer immunotherapy target. Nature. 2017;547(7664):413–8. [PubMed: 28723893]

8. Champiat S, Dercle L, Ammari S, Massard C, Hollebecque A, Postel-Vinay S, et al. Hyperprogressive Disease Is a New Pattern of Progression in Cancer Patients Treated by Anti-PD-1/PD-L1. Clinical cancer research : an official journal of the American Association for Cancer Research. 2017;23(8):1920–8. [PubMed: 27827313]
9. Kato S, Goodman A, Walavalkar V, Barkauskas DA, Sharabi A, and Kurzrock R. Hyperprogressors after Immunotherapy: Analysis of Genomic Alterations Associated with Accelerated Growth Rate. Clinical cancer research : an official journal of the American Association for Cancer Research. 2017;23(15):4242–50. [PubMed: 28351930]
10. Hugo W, Zaretsky JM, Sun L, Song C, Moreno BH, Hu-Lieskovan S, et al. Genomic and Transcriptomic Features of Response to Anti-PD-1 Therapy in Metastatic Melanoma. Cell. 2017;168(3):542.
11. Sharon E. Can an Immune Checkpoint Inhibitor (Sometimes) Make Things Worse? Clinical cancer research : an official journal of the American Association for Cancer Research. 2017;23(8):1879–81. [PubMed: 28258060]
12. Lulli D, Carbone ML, and Pastore S. Epidermal growth factor receptor inhibitors trigger a type I interferon response in human skin. Oncotarget. 2016;7(30):47777–93. [PubMed: 27322144]
13. Morton JJ, Bird G, Keysar SB, Astling DP, Lyons TR, Anderson RT, et al. XactMice: humanizing mouse bone marrow enables microenvironment reconstitution in a patient-derived xenograft model of head and neck cancer. Oncogene. 2016;35:290–300. [PubMed: 25893296]
14. Morton JJ, Keysar SB, Perrenoud L, Chimed TS, Reisinger J, Jackson B, et al. Dual use of hematopoietic and mesenchymal stem cells enhances engraftment and immune cell trafficking in an allogeneic humanized mouse model of head and neck cancer. Mol Carcinog. 2018.
15. Spranger S, Spaapen RM, Zha Y, Williams J, Meng Y, Ha TT, et al. Up-regulation of PD-L1, IDO, and T(regs) in the melanoma tumor microenvironment is driven by CD8(+) T cells. Sci Transl Med. 2013;5(200):200ra116.
16. Spranger S, Bao R, and Gajewski TF. Melanoma-intrinsic beta-catenin signalling prevents anti-tumour immunity. Nature. 2015;523(7559):231–5. [PubMed: 25970248]
17. Keysar SB, Astling DP, Anderson RT, Vogler BW, Bowles DW, Morton JJ, et al. A patient tumor transplant model of squamous cell cancer identifies PI3K inhibitors as candidate therapeutics in defined molecular bins. Molecular oncology. 2013;7(4):776–90. [PubMed: 23607916]
18. Bolger AM, Lohse M, and Usadel B. Trimmomatic: a flexible trimmer for Illumina sequence data. Bioinformatics. 2014;30(15):2114–20. [PubMed: 24695404]
19. Hintzsche J, Kim J, Yadav V, Amato C, Robinson SE, Seelenfreund E, et al. IMPACT: a whole-exome sequencing analysis pipeline for integrating molecular profiles with actionable therapeutics in clinical samples. J Am Med Inform Assoc. 2016;23(4):721–30. [PubMed: 27026619]
20. Sherry ST, Ward MH, Kholodov M, Baker J, Phan L, Smigielski EM, et al. dbSNP: the NCBI database of genetic variation. Nucleic acids research. 2001;29(1):308–11. [PubMed: 11125122]
21. Genomes Project C, Auton A, Brooks LD, Durbin RM, Garrison EP, Kang HM, et al. A global reference for human genetic variation. Nature. 2015;526(7571):68–74. [PubMed: 26432245]
22. Trapnell C, Roberts A, Goff L, Pertea G, Kim D, Kelley DR, et al. Differential gene and transcript expression analysis of RNA-seq experiments with TopHat and Cufflinks. Nature protocols. 2012;7(3):562–78. [PubMed: 22383036]
23. Mootha VK, Lindgren CM, Eriksson KF, Subramanian A, Sihag S, Lehar J, et al. PGC-1alpha-responsive genes involved in oxidative phosphorylation are coordinately downregulated in human diabetes. Nat Genet. 2003;34(3):267–73. [PubMed: 12808457]
24. Liberzon A, Birger C, Thorvaldsdottir H, Ghandi M, Mesirov JP, and Tamayo P. The Molecular Signatures Database (MSigDB) hallmark gene set collection. Cell Syst. 2015;1(6):417–25. [PubMed: 26771021]
25. Yu G, Wang LG, Han Y, and He QY. clusterProfiler: an R package for comparing biological themes among gene clusters. OMICS. 2012;16(5):284–7. [PubMed: 22455463]
26. Love MI, Huber W, and Anders S. Moderated estimation of fold change and dispersion for RNA-seq data with DESeq2. Genome biology. 2014;15(12):550. [PubMed: 25516281]

27. Huang da W, Sherman BT, and Lempicki RA. Systematic and integrative analysis of large gene lists using DAVID bioinformatics resources. Nature protocols. 2009;4(1):44–57. [PubMed: 19131956]
28. Huang da W, Sherman BT, and Lempicki RA. Bioinformatics enrichment tools: paths toward the comprehensive functional analysis of large gene lists. Nucleic acids research. 2009;37(1):1–13. [PubMed: 19033363]
29. Le PN, Keysar SB, Miller B, Eagles JR, Chimed TS, Reisinger J, et al. Wnt signaling dynamics in head and neck squamous cell cancer tumor-stroma interactions. Mol Carcinog. 2019;58(3):398–410. [PubMed: 30378175]
30. Keysar SB, Le PN, Miller B, Jackson BC, Eagles JR, Nieto C, et al. Regulation of Head and Neck Squamous Cancer Stem Cells by PI3K and SOX2. J Natl Cancer Inst. 2017;109(1).
31. Jimeno A, Feldmann G, Suarez-Gauthier A, Rasheed Z, Solomon A, Zou GM, et al. A direct pancreatic cancer xenograft model as a platform for cancer stem cell therapeutic development. Molecular cancer therapeutics. 2009;8(2):310–4. [PubMed: 19174553]
32. Sugimoto K, Adachi Y, Moriyama K, Qiong W, Nakayama A, Hosono M, et al. Induction of the expression of SCF in mouse by lethal irradiation. Growth Factors. 2001;19(4):219–31. [PubMed: 11811778]
33. Barker JN, Scaradavou A, and Stevens CE. Combined effect of total nucleated cell dose and HLA match on transplantation outcome in 1061 cord blood recipients with hematologic malignancies. Blood. 2010;115(9):1843–9. [PubMed: 20029048]
34. Burd CE, Liu W, Huynh MV, Waqas MA, Gillahan JE, Clark KS, et al. Mutation-specific RAS oncogenicity explains NRAS codon 61 selection in melanoma. Cancer Discov. 2014;4(12):1418–29. [PubMed: 25252692]
35. Johnson DB, Lovly CM, Flavin M, Panageas KS, Ayers GD, Zhao Z, et al. Impact of NRAS mutations for patients with advanced melanoma treated with immune therapies. Cancer Immunol Res. 2015;3(3):288–95. [PubMed: 25736262]
36. Wang Y, Velho S, Vakiani E, Peng S, Bass AJ, Chu GC, et al. Mutant N-RAS protects colorectal cancer cells from stress-induced apoptosis and contributes to cancer development and progression. Cancer Discov. 2013;3(3):294–307. [PubMed: 23274911]
37. Avalle L, Pensa S, Regis G, Novelli F, and Poli V. STAT1 and STAT3 in tumorigenesis: A matter of balance. JAKSTAT. 2012;1(2):65–72. [PubMed: 24058752]
38. McConnell AT, Ellis R, Pathy B, Plummer R, Lovat PE, and O'Boyle G. The prognostic significance and impact of the CXCR4-CXCR7-CXCL12 axis in primary cutaneous melanoma. Br J Dermatol. 2016;175(6):1210–20. [PubMed: 27167239]
39. Cowey CL, Liu FX, Black-Shinn J, Stevinson K, Boyd M, Frytak JR, et al. Pembrolizumab Utilization and Outcomes for Advanced Melanoma in US Community Oncology Practices. Journal of immunotherapy. 2017.
40. Achkar T, and Tarhini AA. The use of immunotherapy in the treatment of melanoma. J Hematol Oncol. 2017;10(1):88. [PubMed: 28434398]
41. Heppt MV, Steeb T, Schlager JG, Rosumeck S, Dressler C, Ruzicka T, et al. Immune checkpoint blockade for unresectable or metastatic uveal melanoma: A systematic review. Cancer Treat Rev. 2017;60:44–52. [PubMed: 28881222]
42. Liu B, Song Y, and Liu D. Recent development in clinical applications of PD-1 and PD-L1 antibodies for cancer immunotherapy. J Hematol Oncol. 2017;10(1):174. [PubMed: 29195503]
43. Bai J, Gao Z, Li X, Dong L, Han W, and Nie J. Regulation of PD-1/PD-L1 pathway and resistance to PD-1/PD-L1 blockade. Oncotarget. 2017;8(66):110693–707. [PubMed: 29299180]
44. Jespersen H, Lindberg MF, Donia M, Soderberg EMV, Andersen R, Keller U, et al. Clinical responses to adoptive T-cell transfer can be modeled in an autologous immune-humanized mouse model. Nat Commun. 2017;8(1):707. [PubMed: 28955032]
45. Lin S, Huang G, Cheng L, Li Z, Xiao Y, Deng Q, et al. Establishment of peripheral blood mononuclear cell-derived humanized lung cancer mouse models for studying efficacy of PD-L1/PD-1 targeted immunotherapy. MAbs. 2018;10(8):1301–11. [PubMed: 30204048]
46. Morton JJ, Alzofon N, and Jimeno A. The humanized mouse: Emerging translational potential. Mol Carcinog. 2020.

47. Danner R, Chaudhari SN, Rosenberger J, Surls J, Richie TL, Brumeanu TD, et al. Expression of HLA class II molecules in humanized NOD.Rag1KO.IL2RgcKO mice is critical for development and function of human T and B cells. PloS one. 2011;6(5):e19826. [PubMed: 21611197]

48. Patton J, Vuyyuru R, Siglin A, Root M, and Manser T. Evaluation of the efficiency of human immune system reconstitution in NSG mice and NSG mice containing a human HLA.A2 transgene using hematopoietic stem cells purified from different sources. Journal of Immunological Methods. 2015;422:13–21. [PubMed: 25776756]

49. Morton JJ, Bird G, Refaeli Y, and Jimeno A. Humanized Mouse Xenograft Models: Narrowing the Tumor-Microenvironment Gap. Cancer research. 2016;76(21):6153–8. [PubMed: 27587540]

50. Chen P, Huang Y, and Womer KL. Effects of mesenchymal stromal cells on human myeloid dendritic cell differentiation and maturation in a humanized mouse model. Journal of Immunological Methods. 2015;427:100–4. [PubMed: 26522667]

51. Coulson-Thomas VJ, Gesteira TF, Hascall V, and Kao W. Umbilical cord mesenchymal stem cells suppress host rejection: the role of the glycocalyx. J Biol Chem. 2014;289(34):23465–81. [PubMed: 24986866]

52. Teicher BA, and Fricker SP. CXCL12 (SDF-1)/CXCR4 pathway in cancer. Clinical cancer research : an official journal of the American Association for Cancer Research. 2010;16(11):2927–31. [PubMed: 20484021]

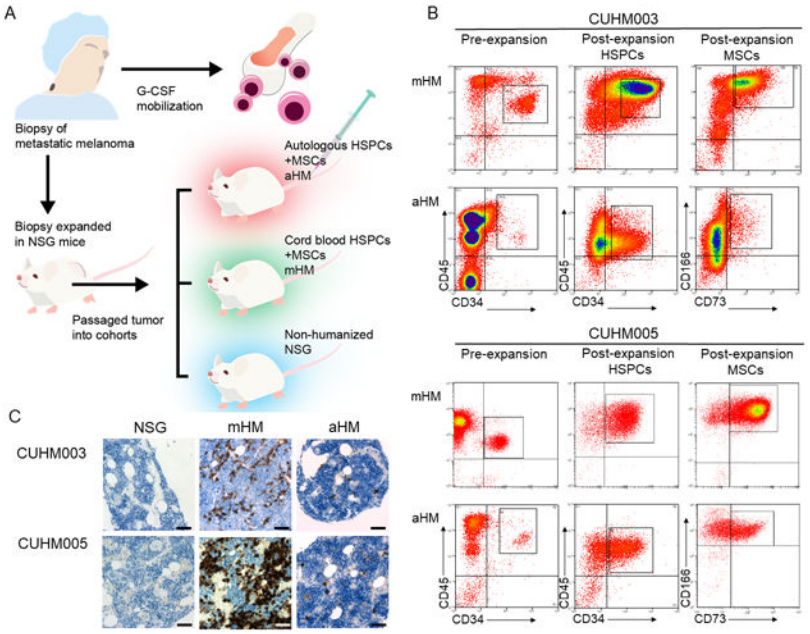

Figure 1: Generation of autologous humanized mice (aHM).

(A) An overview of how aHM cohorts can be generated to investigate patient therapy. G-CSF-stimulated HSPCs from melanoma patients can reconstitute their immune system in immunocompromised mice. Patient tumors can be implanted onto the flanks and shoulder of these mice, as well as onto concurrently prepared mHM and NSG controls. All mice can be treated with the same therapies administered to the patient and their tumor responses compared. **(B)** *In vitro* culture and expansion of cord- and patient-derived HSPC and MSC-like cell populations. Following CD34+ column selection, analysis by cell cytometry identifies a small population of CD34+45+ HSPCs in both the newly procured cord (mHM003 or mHM005) and patient (aHM003 or aHM005) blood. After 5-8 days of expansion, the CD34+ HSPC population has increased markedly for all of these cultures. A population of CD34-, CD73+166+ adherent MSC-like cells originating from within the HSPC population can also be identified after *in vitro* expansion. Total cell numbers of HSPCs before and after expansion are recorded in Supplemental Table 1. **(C)** Representative IHC showing the relative populations of human CD45+ cells (dark brown) within the bone marrow of NSG, mHM, and aHM CUHM003 and CUHM005 models. Magnification is 20x; scale bar = 50 μm.

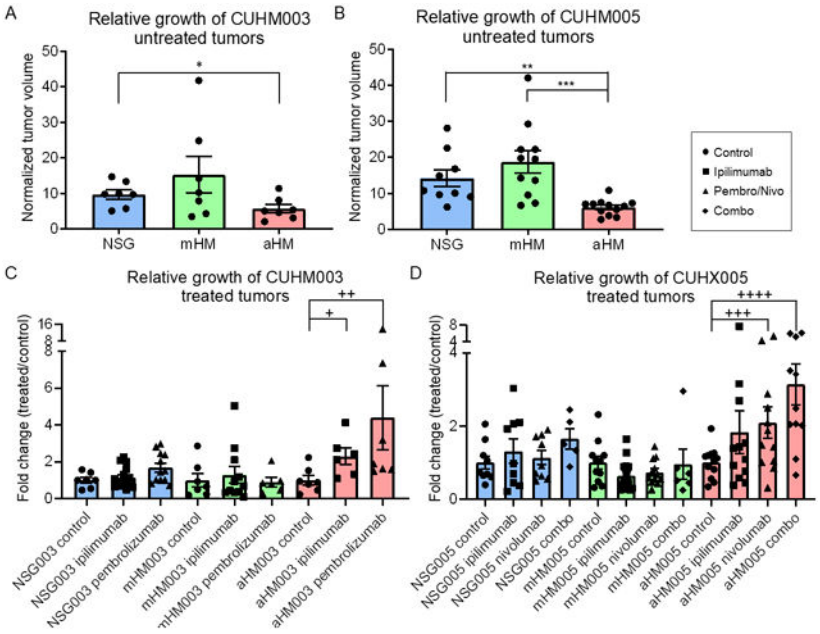

Figure 2: Tumor growth dynamics are significantly impacted in aHM models.

(A-B) Relative growth rates of untreated CUHM003 and CUHM005 tumors in the NSG, mHM, and aHM models. CUHM003 tumors implanted on aHM (n=7) grew significantly slower than those implanted on NSG mice (n=7; *p=0.04, by two-sided t test for this and all subsequent comparisons). CUHM005 tumors implanted on aHM (n=12) grew more slowly than those implanted in either mHM (n=11; **p<0.01) or NSG mice (n=9; ***p<0.01). **(C)** For CUHM003, no significant change in tumor growth was observed in response to ipilimumab or pembrolizumab treatment in either the NSG (n=15 or 12) or mHM (n=11 or 6) cohorts. However, among the aHM treatment resulted in a varied response (ANOVA; p=0.06) with ipilimumab producing a 2-fold increase in tumor growth (n=6; +p=0.02), while pembrolizumab stimulated more than a 4-fold surge in growth (n=7; ++p=0.08). **(D)** In CUHM005, there was again no difference after ipilimumab, nivolumab, or combination therapy among the NSG (n=9, 9, 5) or mHM (n=15, 12, 6) cohorts. In the aHM, response was again varied (AVONA, p<0.01). Although ipilimumab (n=12) did not stimulate significant tumor growth, nivolumab resulted in a 2-fold increase in growth (n=12; +++p=0.02), and the combination of ipilimumab and nivolumab yielded greater than a 3-fold jump in tumor growth (n=11; ++++p<0.01).

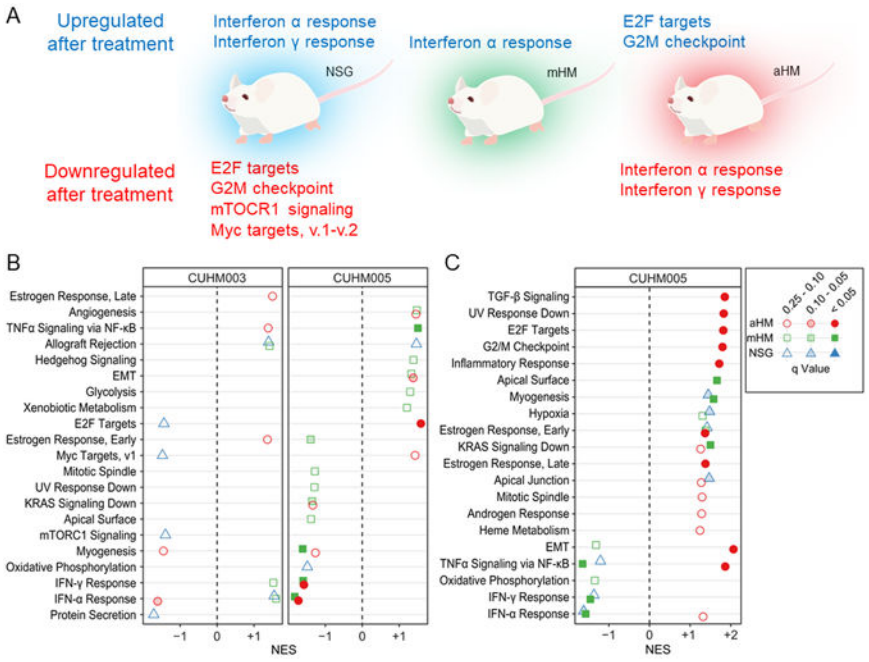

Figure 3: Transcriptome data identifying patterns of gene expression in tumors from humanized mice.

(A) When GSEA hallmark changes due to immunotherapy treatment are considered, IFNα and IFNγ responses rise in NSG and mHM models but fall in aHM, indicating that the genes in this pathway are regulated in a different manner than that occurring in the other models. **(B)** Expression change plot for each GSEA hallmark, showing the relative change in expression after anti-PD-1 treatment for tumors in NSG, mHM, and aHM. Solid points have an adjusted FDR q-value <0.05 and shaded points are <0.10, as determined by a two-sided modified Kolmogorov-Smirnov permutation test. Significant changes can be detected in the IFNα and IFNγ responses. **(C)** Similar expression change plot for CUHM005 showing GSEA changes after combination therapy. Although the EMT and TNFα hallmarks rise in aHM, no further changes in IFN expression are noted.

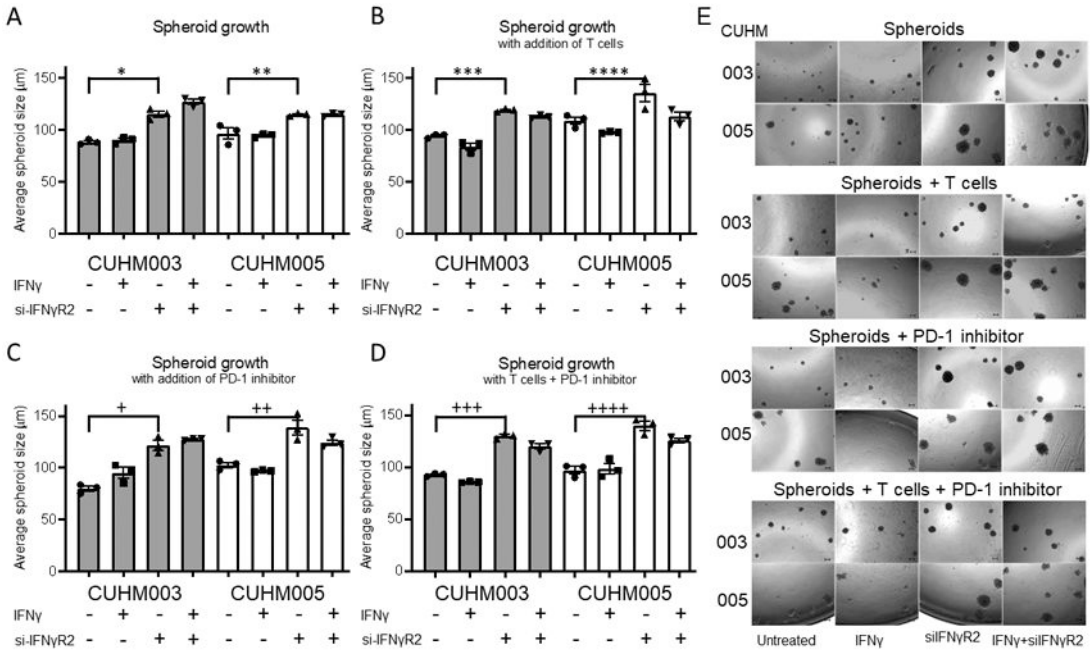

Figure 4: *In vitro* response to depleted IFNγ signaling.

(A) CUHM003 and CUHM005 cell lines were transfected with siRNA against IFNγ receptor 2 (*IFNGR2*) then cultured in triplicate as spheroids in the presence of IFNγ and their sizes recorded and averaged (n~120 colonies per well; three wells per cell line per condition). Although the addition of IFNγ only minimally impacted average spheroid size, cells transfected with an siRNA against the IFNγ receptor formed significantly larger spheroids (ANOVA p=0.001; CUHM003, *p<0.001; CUHM005, **p=0.006 by a Dunnett's comparisons test for this and subsequent comparisons). **(B)** The addition of activated mismatched T cells had a minimal effect on spheroid size but did not alter the observed size increase after IFNγ receptor knockdown (ANOVA p=0.005; CUHM003, ***p<0.001; CUHM005, ****p=0.01). **(C)** Likewise, the addition of a PD-1 inhibitor (pembrolizumab for CUHM003 or nivolumab for CUHM005) did not change spheroid size and did not alter the effect of the IFNγ receptor knockdown (ANOVA p<0.001; CUHM003, +p<0.001; CUHM005, ++p=0.001). **(D)** The addition of both T cells and the corresponding PD-1 inhibitor also only marginally changed sphere size and did not alter the increase in spheroid size induced by IFNγ receptor siRNA knock-down (ANOVA p<0.001; CUHM003 +++p<0.001, CUHM005 ++++p<0.001). **(E)** Representative images showing the comparative sizes of spheroids, spheroids after the addition of IFNγ, and spheroids after transfection with an siRNA against the IFNγ receptor (top panel), as well as observed changes in size resulting from the addition of T cells (second panel), a PD-1 inhibitor (third panel), or of T cells plus a PD-1 inhibitor (bottom panel). Scale bar = 100µm.

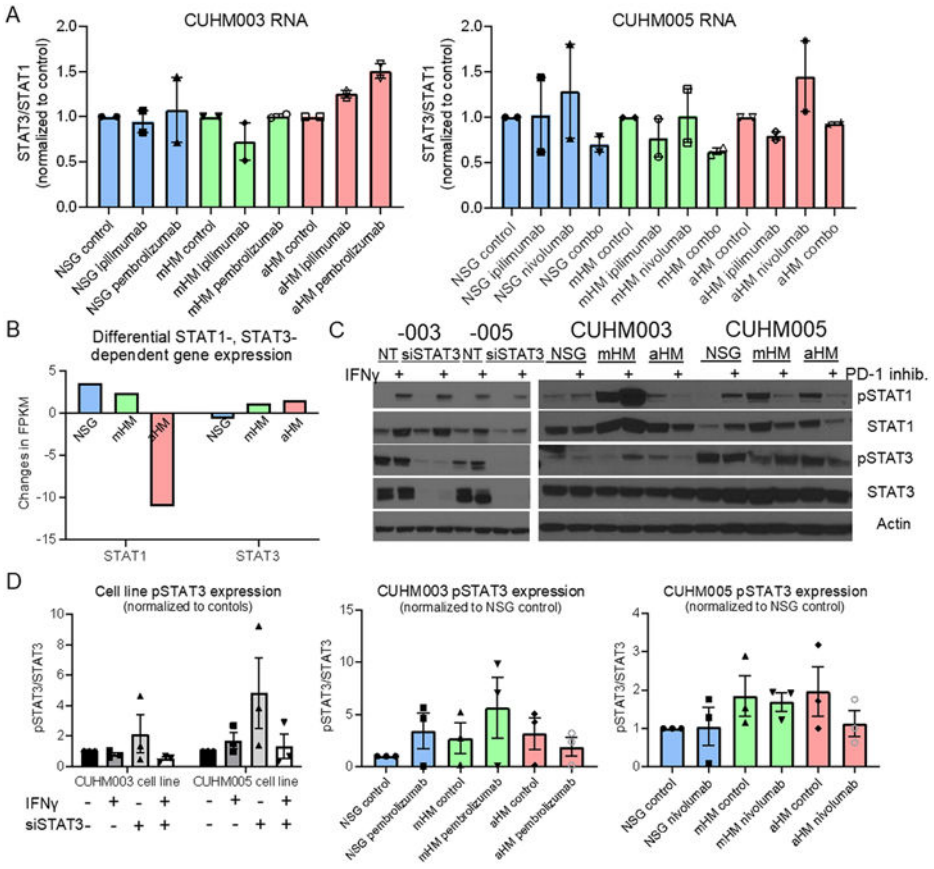

Figure 5: *Ex vivo* examination of Jak-STAT pathway alterations in tumor hyperprogression.

(A) The FPKM values for biological duplicates the STAT3 and STAT1 transcripts were used to determine the ratio of STAT3/STAT1 gene expression in the NSG, mHM, and aHM CUHM003 and CUHM005 control and treated tumors. The pattern of the STAT3/STAT1 ratio corresponds to the pattern of tumor growth observed in the mouse models. **(B)** A compilation of the FPKM values of the genes responsive to STAT1 and STAT3 activation shows changes in STAT1 and STAT3 regulation after PD-1 inhibitor treatment in NSG, mHM, and aHM. Transcription data from both CUHM003 and CUHM005 tumors was combined for each mouse group for this analysis. **(C)** Representative western blots of patient-derived CUHM003 and CUHM005 cell lines (left) or PDX tumor tissue (right), showing the effects of the addition of IFNγ and/or expression of an siRNA STAT3 construct on STAT1 and STAT3 protein expression and phosphorylation (in the cell lines) or the effects of PD-1 inhibitor (in the PDX). pSTAT3 expression is calculated based on total STAT3 expression. **(D)** Densitometry averaged from triplicate western blots shows that pSTAT3 expression (as a fraction of STAT3 expression) decreases after the application of IFNγ to cell lines expressing an siRNA STAT3 construct (final two bars of the left chart) and in aHM tumors treated with pembrolizumab (CUHM003; middle chart) or nivolumab (CUHM005; right chart).

TABLE 1

Percentage of tumor-infiltrating T cells in HM cohorts

CUHM003							
	mHM			aHM			T cell invasive capacity (aHM/mHM)
	BM (%)	T cells (%)	T cells/BM	BM (%)	T cells (%)	T cells/BM	
Control	3.70	0.007	0.002	0.183	0.003	0.014	7.59
Ipilimumab	12.92	0.010	0.001	0.480	0.003	0.005	6.73
Pembrolizumab	14.01	0.095	0.007	0.220	0.003	0.012	1.84
CUHM005							
	mHM			aHM			T cell invasive capacity (aHM/mHM)
	BM (%)	T cells (%)	T cells/BM	BM (%)	T cells (%)	T cells/BM	
Control	44.95	0.01	0.0002	0.01	0.007	0.488	2192
Ipilimumab	27.46	0.01	0.0004	0.04	0.013	0.357	981
Nivolumab	19.26	0.01	0.0005	0.04	0.007	0.168	324
Combination	20.07	0.01	0.0005	0.06	0.002	0.030	61